Pan Xiao (Orcid ID: 0000-0001-8578-717X)

Cause of an extreme warm and rainy winter in Shanghai in 2019

Xiao Pan[1], Wei Wang[2], Tim Li[3, 1*], Fei Xin[4] and Jinhua Yu[1*]

1. Key Laboratory of Meteorological Disaster, Ministry of Education (KLME) / Joint International Research Laboratory of Climate and Environmental Change (ILCEC) / Collaborative Innovation Center on Forecast and Evaluation of Meteorological Disasters (CIC-FEMD), Nanjing University of Information Science and Technology, Nanjing, 210044, China

2. Minhang Meteorological Bureau, Shanghai, 201199, China

3. Department of Atmospheric Sciences, School of Ocean and Earth Science and Technology, University of Hawaii, Honolulu, Hawaii, HI96822, USA

4. Shanghai Climate Center, Shanghai, 200030, China

Corresponding author:

Tim Li, Department of Atmospheric Sciences, School of Ocean and Earth Science and Technology, University of Hawaii at Manoa, Honolulu, Hawaii 96822. Email: timli@hawaii.edu

Jinhua Yu, Nanjing University of Information Science and Technology, Ningliu Road 219, Meteorology Bldg. Jiangsu 210044, China. E-mail: jhyu@nuist.edu.cn

This is the author manuscript accepted for publication and has undergone full peer review but has not been through the copyediting, typesetting, pagination and proofreading process, which may lead to differences between this version and the Version of Record. Please cite this article as doi: 10.1002/joc.7094

Abstract

An extreme warm winter (ranked first during the past 30 years) occurred in Shanghai in 2019, accompanied with an extreme rainy winter (ranked thirdly in the same period). An observational diagnosis shows that the extreme warm and rainy winter arose from southerly anomalies associated with an anticyclone east of Shanghai. The cause of the anticyclone was attributed to V-shaped upper-tropospheric Rossby wave activity fluxes, originated from the North Atlantic and tropical Indian Ocean. Numerical model experiments indicate that the anomalous heat source in the tropical Indian Ocean played a dominant role (~65%) in causing the local anomalous circulation, while the heating in North Atlantic also played a role (~35%).

A further analysis of the past 30 year data revealed that an extreme warm winter in the past did not coincide with an extreme wet winter. While the warm winter composite shows a large-scale anticyclone anomaly over Central and East Asia, the rainy winter composite exhibits a circulation dipole pattern with an anomalous cyclone (anticyclone) west (east) of Shanghai. Numerical experiments confirm that the former was forced by the combined effect of precipitation anomalies over the North Atlantic and tropical Indian Ocean (IO) and Maritime Continent (MC) through Rossby wave energy dispersion, whereas the latter was caused by a dipole heating pattern over the tropical IO/MC sector.

Keywords

Extreme warm winter; Extreme rainy winter; Tropical forcing; Rossby wave train; Rossby wave activity flux.

1. Introduction

Shanghai is a world-renewed metropolis and one of the biggest commercial cities in China. Located in the eastern coast of China, it owns the unique climate which is important for local human activities and economic development. In 2019, Shanghai experienced an anomalous warm and rainy winter and the cause of the unusual temperature and precipitation is eager to be explored.

Previous studies revealed that various climate systems could affect the winter climate in East China, including tropical and extratropical teleconnections. For instance, the El Niño-southern Oscillation (ENSO) may modulate the temperature and rainfall in Southeast China through anomalous Walker circulation and anomalous western North Pacific anticyclone (cyclone) (e.g., Zhang et al., 1996; Wang et al., 2000; Wu et al., 2017; for a thorugh review, readers is referred to Li et al., 2017). A long persistent rainy winter in Shanghai in 2018 was at least partly attributed to the ENSO forcing (Wang et al., 2020; Liu et al., 2020). When El Niño occurred in phase with Pacific Decadal Oscillation (PDO), an anomalous warm temperature often occurred in East China (Kim et al., 2014).

The East Asian winter monsoon (EAWM) is another important system that affects winter rainfall and temperature over East and Southeast China (e.g., Wang and Feng, 2011; Lee et al., 2013). Several studies showed that a positive phase of the Arctic Oscillation (AO) could weaken the strength of EAWM through impacting the Siberian High, mid-latitude westerlies and Rossby wave activities (Wu and Wang, 2002; Suo et al., 2009; Chen and Zhou, 2012; Tan and Chen, 2014; He et al., 2017), which led to a warm winter in East China. The pressure systems associated with the North Pacific Oscillation (NPO) could affect the climate in Northeast China through its westward expansion (Rogers, 1981; Wang et al., 2011). Besides, the signals in Atlantic, including

the North Atlantic Oscillation (NAO; Wu et al., 2009), the North Atlantic triple SSTA pattern (Zhou, 2013) and the Atlantic Meridional Overturning Circulation (Sun et al., 2012), could also affect the EAWM. An 11-yr solar cycle might modulate the relationship between AO/NAO and EAWM (Zhou et al., 2013).

Additionally, the Eurasia teleconnection (Wallace and Gutzler, 1981) played a role in causing the extreme temperature and rainfall in China (Huang et al., 2006), such as a record-breaking long-lasting cold winter in 2008 (Wen et al., 2009). The tropical Indian Ocean SST may affect climate in East Asia via atmospheric teleconnection (Ueda et al., 2015). The Tibetan Plateau and Mongolian Plateau may exert a dynamic impact on East Asia climate (Zhang et al., 2015; Sha et al., 2015).

Figure 1 shows that Shanghai experienced an extremely warm and rainy winter (December, January, February) in 2019. Note that the DJF mean temperature in 2019 is highest during the past 30 years, while the winter mean precipitation ranks thirdly during the same period. What caused an extreme warm and rainy winter in 2019? What are difference and similarity between the circulation anomaly in 2019 and those in historical warm and rainy winters in the past 30 years? The objective of the current study is to address the questions above. The remaining part of this paper is organized as follows. Section 2 introduces observational data and methods used and designed numerical model experiments. Section 3 describes the observed circulation charateristics in 2019 and discusses the physical mechanism responsible for the extreme warm and rainy winter. In Section 4 we further examine the circulation patterns associated with historical extreme warm and rainy winters during the past 30 years and associated physical processes. Finally a conclusion and discussion are given in Section 5.

2. Data, method and model experiments

2.1 Data

The datasets we used in the paper include: 1) monthly observed temperature and precipitation data from 11 main stations in Shanghai; 2) monthly data of air temperature, horizontal wind, vertical velocity, geopotential height and relative humidity fields derived from the National Centers for Environmental Prediction/Department of Energy (NCEP/DOE) Reanalysis II (Kanamitsu et al., 2002) at a 2.5º×2.5º horizontal resolution; 3) monthly precipitation data from National Oceanic and Atmospheric Administration (NOAA) Climate Prediction Center Merged Analysis of Precipitation (CMAP) with a 2.5º×2.5º horizontal resolution (Xie and Arkin, 1997). All the datasets cover the period of 1990-2019.

The correlation coefficients between the precipitation (temperature) averaged over 11 observational stations in Great Shanghai City and the merged CMAP precipitation dataset (NCEP2 reanalysis dataset) from 1990 to 2019 shows that the precipitation (temperature) averaged over Shanghai 11 stations are significantly correlated with that over a large area of East China (figure not shown). Therefore, the precipitation (temperature) time series shown in Fig. 1 represents well large-scale climate conditions over East China.

2.2 Method

The moist static energy (MSE; Wang et al., 2017; see equation 1) can describe the atmospheric moisture and temperature characteristics.

$$MSE = C_p T + gz + L_v q, \quad (1)$$

where T, z and q represent the temperature, height and specific humidity. $C_p (= 1004\, J \cdot kg^{-1} \cdot K^{-1})$ is the specific heat at constant pressure, $g (= 9.8\ m \cdot s^{-2})$ is the

gravitational acceleration and $L_v(= 2.5 \times 10^6\, J \cdot kg^{-1})$ is the latent heat of vaporization.

To describe the propagation of Rossby wave energy in the upper troposphere, a phase-independent wave activity flux (WAF; Takaya and Nakamura, 2001; see equation 2 below) was calculated. The phase-independent flux was derived from combined perturbation energy and pseudo momentum terms. The so-derived WAF is parallel to the group velocity of local Rossby waves, and is suitable for a snapshot analysis of either stationary or migratory waves on a zonally varying basic flow. Thus the WAF represents the propagation of the wave packet and its divergence (convergence) represents the source (sink) of the wave packet. Mathematically, the WAF can be written as:

$$\boldsymbol{W} = \frac{1}{2|\bar{U}|}\begin{bmatrix}\bar{u}(\psi_x'^2 - \psi'\psi_{xx}') + \bar{v}\left(\psi_x'\psi_y' - \psi'\psi_{xy}'\right) \\ \bar{u}\left(\psi_x'\psi_y' - \psi'\psi_{xy}'\right) + \bar{v}\left(\psi_y'^2 - \psi'\psi_{yy}'\right)\end{bmatrix}, \quad (2)$$

where $|\bar{\boldsymbol{U}}|$, $\bar{u}$, $\bar{v}$ are mean state wind speed, zonal and meridional wind, ψ' is the perturbation stream function, and the subscript of ψ' denotes the partial derivative of ψ' at either zonal or meridional directions. In the current calculation, the anomaly wind field in 2019 is considered as the perturbation part and the climatological mean of 1990-2019 is considered as the mean state.

The specific humidity is calculated based on $q = \frac{0.622 \cdot RH \cdot e_s}{p - 0.378 e_s}$, where $e_s = 6.112 \cdot exp(\frac{17.67t}{t+243.5})$ denotes the saturated vapor pressure, *q*, *RH*, *p* and *t* represent the specific humidity, relative humidity, pressure and air temperature.

2.3 Model Experiments

An atmospheric general circulation model, the ECHAM version 4.6 (hereafter ECHAM4.6) developed by Max-Plank Institute for Meteorology (Roeckner et al.,

1996), is used to investigate the atmospheric circulation response to a specified anomalous heat source. It is based on the primitive equations and has a 2.8° ×2.8° (T42) horizontal resolution with 19 vertical levels in a hybrid sigma pressure coordinate system (from surface to 10hPa). By designing sensitivity experiments, we aim to understand the relative contributions of different heat sources in causing the formation of the anomalous anticyclone over southern Japan. This model was previously used for examining the tropics – mid-latitude teleconnection (Zhu et al., 2014; Zhu et al., 2016; Jiang and Li, 2019) and the dynamics of the Madden-Julian Oscillation (Wang et al., 2017).

In the control (CTRL) experiment, ECHAM4.6 was forced by the observed climatological monthly mean SST for a 30-year period. In the sensitivity (SEN) experiments, an anomalous heating field resembling the observed precipitation pattern over a specified region was specified under the climatological mean SST. The vertical profile of the heating was specified as a linear function of pressure with a maximum heating rate at 300hPa. The difference between SEN and CTRL represents the atmospheric response to the specified heating anomaly.

3. Cause of the extreme warm and rainy winter in 2019

To understand the cause of the extreme warm and rainy winter in 2019, we examine the horizontal patterns of anomalous air temperature, specific humidiy, MSE, horizontal and vertical velocity fields (Fig. 2). Positive temperature and moisture anomalies appeared in Shanghai and surrounding area (Figs. 2a, 2b). The increase of local temperature and moisture led to an increase of low-level MSE as seen from the horizontal pattern of 1000hPa-850hPa integrated MSE anomaly (Fig. 2c). Given that most of the precipitation in East China in winter is synoptic frontal precipitation, an

enhanced background seasonal mean moisture in Shanghai could strengthen the frontal precipitation, leading to an abnormal wet condition in Shanghai in 2019. In addition to the local anomalies, large-scale positive temperature and moisture anomalies also appeared over the high-latitude Eurasian Continent (Figs. 2a, 2b).

The cause of the local temperature and moisture anomalies was attributed to anomalous southeastlies over East China, as seen from the anomalous low-level wind field (Fig. 2a) and anomalous temperature and moisture advection fields. Figure 3 shows the advection of the mean temperature ($-\boldsymbol{V}'\cdot\nabla\bar{T}$) and the mean moisture ($-\boldsymbol{V}'\cdot\nabla\bar{q}$) by anomalous wind field at 1000hPa. It shows clearly that the anomalous southeasterly wind advected mean state warm and wet air from the south to Shanghai, contributing to the warm and moist winter. Besides, a local warming SSTA appears in West Pacific (Fig. 4c), so the southeasterly wind could advect anomalous warm air to Shanghai. Both the mean warm air and anomalous warm air advected by anomalous wind fields contributed to the warming and moistening in situ. Thus, it is concluded that the anomalous low-level southeasterly played a critical role in the formation of the extreme warm and rainy winter in 2019.

Given the pronounced climatological northerly in northern winter, a natural question is what caused the anomalous southeasterly wind near Shanghai? Figure 2a shows that the southeasterly was a part of an anomalous anticyclone centered at (40°N, 140°E) near Japan. Meanwhile, in the upper troposphere, there were an anomalous positive geopotential height anomaly and an anomalous anticyclone over the same region (Fig. 4a). The equivilant barotropic vertical structure of the local anomalous circulation with greater amplitude in the upper troposphere suggested that the origin of the low-level circulation might arise from the upper-tropospheric forcing.

To explore the cause of the anomalous anticyclone in the upper troposphere, we calculated the Rossby wave activity flux (Fig. 4a). A V-shaped wave train pattern appeared in the upper troposphere over the Eurisian Continent. The wave activity flux firstly emanated southeastward from North Atlantic to northern Indian Ocean and then pointed northeastward from northern Indian Ocean to Japan (Fig. 4a). It is speculated that the two branches of upper-tropospheric Rossby wave activity fluxes had different origins, as seen from the precipitation anomaly pattern (Fig. 4b). One source originated from the tropical Indian Ocean (purple box in Fig. 4b), where there is a positive precipitation anomaly. Accoding to Gill (1980), the positive heating anomaly might induce a positive geopotential height anomaly in the upper troposphere over northern Indian Ocean. Such a upper-level perturbation anomaly further perturbed the westerly jet, exciting a Rossby wave train with an alternated "Anticyclone – Cyclone – Anticyclone" pattern. Through the Rossby wave energy dispersion, an anomalous anticyclone appeared over Japan. Another heat source appeared over the North Atlantic/Europe sector. A positive precipitation anomaly there possibly induced an upper-tropospheric anticyclone in situ, and emanated Rossby wave activity fluxes southeastward. The combination of the two heat sources led to the formation of the V-shaped wave train pattern.

To validate the hypothesis above, a set of idealized numerical model experiments were conducted, with the use of the ECHAM4.6. In the first sensitivity experiment (Sen1_1), the observed precipitation (or heating) anomalies in both the tropical Indian Ocean (10°S-20°N, 40°-80°E) and North Atlantic (50°-60°N, 10°W-10°E) were specified. In the second sensitivity experiment (Sen1_2), only the observed precipitation anomaly in the Indian Ocean (10°S-20°N, 40°-80°E) was specified. In the

third sensitivity experiment (Sen1_3), only the precipitation anomaly in North Atlantic (50°-60°N, 10°W-10°E) was specified. While the horizontal pattern of the specified heating anomaly was exactly from the observed precipitation pattern (shown in Fig. 4b), an idealized vertical profile with a maximum at 300hPa was specified.

Figure 5a shows the horizontal patterns of simulated geopotential height and wind fields at 200 hPa in reponse to both the positive heatings in the Indian Ocean and North Atlantic. A Rossby wave train pattern similar to the observed "V"-shape structure was simulated. As a result, a strong anomalous anticyclone appeared over the East Asia coast near Japan. In contrast, only part of the observed V-shaped wave train was simulated when only one of the two heating sources was specified (Figs. 5b, 5c). Compared to the strength of the anomalous anticyclone over Japan in Sen1_1 (Fig. 5a), the simulated anticyclones in Sen1_2 (Fig. 5b) and Sen1_3 (Fig. 5c) were too weak. Therefore, the numerical model experiments suggested that both of the heating sources in the Indian Ocean and North Atlanric contributed to the formation of the anomalous anticyclone over Japan.

To quantitatively measure the relative contribution of the two heating sources, the simulated southeasterly speeds averaged over (25°-35°N, 110°-130°E) were calculated and compared. The wind speeds in Sen1_1, Sen1_2 and Sen1_3 are 4.6 $m \cdot s^{-1}$, 3.0 $m \cdot s^{-1}$ and 1.6 $m \cdot s^{-1}$ repectively. This implies that the tropical Indian Ocean forcing contributed 65% of the circulation anomaly over East Asia, while the North Atlantic forcing accouts for 35%. A further examination shows that the anomalous precipitation over the tropical Indian Ocean was closely related to underlying anomalous SST pattern (Fig. 4c). Given the persistence of the anomalous SST, the Indian Ocean heat source may be considered as one of predictors for seasonal climate prediction in Shanghai.

One may wonder the effect of positive precipiptation anomaly in central Pacific (Fig. 4b) on the formation of anomalous anticyclone over southern Japan. Another numerical sensitivity experiment was carried out to validate the role of positive heating (precipitation) in central Pacific, which confirmed it played no positive contribution to the generation of anomalous anticyclone (figure not shown).

4. Analyses of extreme warm and rainy winters during the past 30 years

In the analysis above, we focus on the cause of the extreme warm and rainy winter in 2019. Did the similar circulation anomaly happen during the past extreme warm and rainy winters? To address this question, the correlation coefficient between the observed temperature and precipitation anomalies in Shanghai during 1990-2019 was calculated. It is 0.26, which does not pass the 95% confidence level (using t-test). This implies that an anomalous warm winter did not coincide with an anomalous wet winter prior to 2019. Therefore, in the following the analyses of extreme warm and rainy years are studied separately.

Figure 6 shows the standardized time series of the temperature and precipitation anomalies in Shanghai during 1990-2019. The extreme warm and wet winters are defined when the seasonal mean temperature and precipitation anomalies exceed one standard deviation respectively. The result shows that prior to 2019, there were five extreme warm winters that include 1998, 2000, 2001, 2006 and 2016; there were three extreme rainy winters (1997, 2004 and 2018). There is no overlapping between the extreme warm and rainy winters. In the following, we will examine the composite circulation anomalies associated with the extreme warm and rainy winters respectively.

4.1 Extreme warm winter composite

Figure 7a shows the composite low-level wind, geopotential height and temperature fields for the five extreme warm winters (1998, 2000, 2001, 2006 and 2016). A large-scale positive temperature anomaly appeared in Central and East Asia. The warm anomaly was approximately in phase with a large-scale anomalous anticyclone in upper troposphere (Fig. 7b), and was located to the northwest of or in phase with an anomalous anticyclone at low-level. While the low-level southwesterly to the northwest of the anomalous anticyclone induced a warm advection, Ekman pumping induced descent caused an adiabatic warming, leading to a warm and dry condition (Figs. 7a, 7c).

The low-level wind anomaly in Shanghai was dominant by the easterly wind (Fig. 7a), which may advect Kuroshio warm SST to Shanghai and is different from that in 2019 (Fig. 2a). In addition, the wave train pattern at 200hPa (Fig. 7b) also distinguished from that in 2019. To explain the generation of the large-scale anticyclone over Central and East Asia, the composite WAF of the five extreme warm winter was shown in Fig. 7b. In the high-latitudes, a wave train pattern with northeastward and southeastward WAFs was observed, possibly caused by an anomalous heat source (i.e., a positive precipitation anomaly) in North Atlantic (Fig. 7c). In the extratropics, northward WAFs appeared in the longitudinal band of 60°-140°E. The WAFs appeared linking to precipitation anomalies over the tropical Indian Ocean/Maritime Continent (IO/MC) sector (Fig. 7c).

To test the hypothesis that the heating anomalies over the IO/MC sector and North Atlantic induced the large-scale anticyclone in upper troposphere over Central and East Asia, we conducted the second set of sensitivity experiments. In the first experiment (Sen2_1), the observed heating anomalies in both the IO/MC sector (10°S-20°N, 50°-

160°E) and North Atlantic (50°-65°N, 10°W-15°E) were specified. In the second experiment (Sen2_2), only the observed positive precipitation anomaly in MC (10°S-20°N, 90°-160°E) was considered. In the third experiment (Sen2_3), only the negative precipitation anomaly in IO (10°S-20°N, 0°-90°E) was specified. In the fourth experiment (Sen2_4), only the positive heating in North Atlantic (50°-65°N, 10°W-15°E) was specified. The same modeling approach as in the first set of experiments was adopted.

Figure 8 shows the simulated geopotential height and wind fields at 200hPa in the four experiments above. In Sen2_1, the simulated large-scale circulation field (Fig. 8a) was similar to the observation (Fig. 7b), with a marked large-scale anticyclone anomaly appearing over Central and East Asia. A high-latitude wave train pattern resembling the observed was also captured when all the heatings are considered (Fig. 8a). In Sen2_2, with a specified heating only in MC, the model simulated a similar geopotential anomaly pattern in Central and East Asia (Fig. 8b), even though its longitude range was smaller than that of Sen2_1. When a negative heating in IO was specified, the simulated anticyclone center was shifted northeastward, and the intensity of the anticyclone was weaker (Fig. 8c). With the consideration of only the positive heating in North Atlantic, the simulated anomalous anticyclone center shifted westward and was weaker (Fig. 8d).

To sum up, the sensitivity experiments above suggested that the heating anomalies over the IO, MC and North Atlantic all contributed to the formation of the anomalous anticyclone over Central and East Asia. To quantitatively compare the three heatings' contributions to the anomalous climate condition in Shanghai, we introduce a zonal

wind index defined as an average zonal wind anomaly over (25°-40°N, 105°-125°E). The calculated zonal wind index in Sen2_2, Sen2_3 and Sen2_4 is -0.8 $m \cdot s^{-1}$, -1.1 $m \cdot s^{-1}$ and -1.0 $m \cdot s^{-1}$, which roughly accouts for 30%, 35% and 35% of the total conbined response in Sen2_1. Therefore, it follows that the forcings over the North Atlantic and the IO/MC sector could generate a large-scale anticyclone anomaly in Central and East Asia through northeastward-southeastward and northward Rossby wave activity fluxes, and they were responsible for the extreme warm winters in Shanghai.

4.2 Extreme rainy winter composite

The composite temperature and circulation anomalies associated with the three extreme rainy winters (1997, 2004 and 2018) are shown in Figure 9. The most noted feature over East Asia is a zonal dipole pattern with an anomalous cyclone to the west of Shanghai and an anomalous anticyclone to the east (Fig. 9a). While the anomalous cyclone was accompanied by a cold near surface temperature anomaly over East Asia due to Ekman pumping induced adiabatic cooling and the hydrostatic approximation, low-level southerly anomalies to the east of the anomalous cyclone and to the west of the anomalous anticyclone advected higher mean moisture from the south to Shanghai, leading to a positive moisture advection. As a result, a positive specific humidity anomaly belt appeared to the south of Shanghai (Fig. 9b). Whereas the southerly induced warm advection tended to offset the adiabatic cooling effect, the moisture increase led to the increase of local MSE, as seen from Fig. 9c. Enhanced background low level moisture and temperature were conducive to the increase of frontal precipitation, leading to a rainy winter in Shanghai.

The dipole circulation pattern is more clearly seen in the upper troposphere (Fig.

10a). A large-scale anomalous cyclone appeared over the Eurasian Continent, while an anomalous anticyclone with smaller zonal extent appeared to its east. An interesting feature is northeastward WAF, emanated from the tropical Indian Ocean where a positive geopotential height anomaly was located (Fig. 10a). The northeastward WAF linked closely to the precipitation dipole pattern over the tropical IO/MC sector (Fig. 10b).

According to NOAA issued ONI index, all the three years (1997, 2004 and 2018) belong to an El Niño years. Anomalous Walker circulation associated with the El Niños induced anomalous descent over the MC during El Niño mature winters, which was responsible for the negative heating in the MC. The anomalous heating over the MC could further induce anomalous ascent in the western Indian Ocean through an anomalous local Walker cell (Li et al., 2003).

It is hypothesized that the circulation dipole over mid-latitude Asia is induced by the dipole precipitation anomaly over the tropical IO/MC sector. To test the hypothesis, the third set of sensitivity experiments were carried out. The first sensitivity experiment specifies the observed dipole heating pattern in the tropical IO/MC sector (see purple boxes in Fig. 10b) (hereafter called Sen3_1). The second experiment specfies only the negative heating in eastern IO/MC (Sen3_2). The third experiment specifies only the positive heating in tropical western IO (Sen3_3).

The simulated 200hPa geopotential height and wind fields in the three sensitivity experiments are shown in Figure 11. All the three experiments capture, to a large extent, the dipole circulation pattern over mid-latitude Asia, similar to the observed (Fig. 10a). For example, along 40°N, there are clear negative (positive) geopotential height anomalies west (east) of 120°E. All the three experiments reproduced southeasterly

anomalies along 120°E over East Asia coast. The southeasterly anomalies may transport humid air from the south, contributing a local positive precipitation anomaly.

A more careful comparison shows that the anomalous southeasterly appears stronger in Sen 3_2 than Sen3_3, indicating that effect of the negative precipitation anomaly over eastern IO/MC is more important in inducing the local circulation. To quantitatively compare their relative contributions, the same circulaiton index (i.e., the wind speed anomaly averaged over 25°-35°N, 110°-130°E) is used. The calculated index in Sen3_2 and Sen3_3 is 1.8 $m \cdot s^{-1}$ and 0.8 $m \cdot s^{-1}$ repectively, which roughly accouts for 70% and 30% of the total response (Sen3_1). Therefore, we conclude that the dipole heating pattern in the tropical IO/MC sector is responsible for the circulation anomaly and the extreme rainy winters in Shanghai. The negative heating in the MC appeared more important (70%) while the positive heating in tropical western IO also played a role (30%).

5. Conclusion and discussion

The cause of an extreme warm and rainy winter in Shanghai in 2019 was investigated through both an observational analysis and idealized numerical model experiments. It is found that an anomalous anticyclone occurred over southern Japan east of Shanghai. The southeasterly anomaly to the west of the anticyclone advected warmer and wetter air from the south, leading to positive temperature and moisture advection anomalies. The increased background moisture favored enhanced precipitation even given the same synoptic perturbation.

The anomalous anticyclone had a equivilant barotropic structure. In upper troposphere, a V-shaped wave train pattern appeared over Eurasian Continent. A

southeastward Rossby wave activity flux originated from North Atlantic and ended over tropical northern Indian Ocean. A northeastward Rossby wave activity flux originated from the northern Indian Ocean and ended over southern Japan. Both the branches of the wave trains exhibited an “Anticyclone – Cyclone – Anticyclone” pattern. Two anomalous heat sources were identified from the precipitation anomaly field. One was over North Atlantic and another was over northern Indian Ocean.

The impact of the anomalous heat sources on the upper-tropospheric wave trains and the formation of the anomalous anticyclone over southern Japan was examined through an AGCM (ECHAM4.6). Numerical model experiments indicate that the heat source over the northern Indian Ocean plays a dominant role (about 65%) in generating the anomalous anticyclone over southern Japan, while the North Atlantic heat source also played a role (about 35%).

The examination of historical extreme warm and rainy winters in Shangai during the past 30 years shows that the warm winters did not coincide with the wet winters prior to 2019. By composing atmospheric circulation fields during the extreme warm and wet years respectively, we found that a large-scale anomalous anticyclone appeared over mid-latitude Central and East Asia during the warm winter composite. The anticyclone exhibited a quasi-barotropic structure. The warming was primarily caused by Ekman pumping induced descent and associated adiabatic warming process. A set of sensitivity model experiments further validate the role of the heating anomalies over the North Atlantic and the tropical IO/MC sector in generating the anomalous anticyclone in Central and East Asia through Rossby wave energy dispersion.

The composite circulation anomaly associated with the extreme rainy winters prior to 2019 was characterized by a zonal dipole pattern with an anomalous cyclone to the west and an anomalous anticyclone to the east of Shanghai. While the anomalous

cyclone was accompanied by a cold surface temperature anomaly over East Asia, the southerly anomaly west of the anomalous anticyclone advected high mean moisture from the south, leading to a rainy winter in Shanghai. We hypothesized that the circulation dipole over Asia was attributed to a heating dipole over the tropical IO/MC sector. Sensitivity numerical experiments confirm the tropical dipole heating effect. It was primarily attributed to a negative heating over MC (70%), while a positive heating in tropical IO also played a role (30%).

It is interesting to note that the historical extreme rainy winters were accompanied by a typical eastern Pacific El Niño event with a well-established WNPAC (Wang et al., 2003; Li et al., 2017). In contrast, winter in 2019 was associated with a weak central Pacific El Niño. Given an extremely strong Indian Ocean dipole in autumn and a subsequent strong basin wide warming in winter 2019 (figure not shown), the SST and associated precipitation anomalies in tropical Indian Ocean might play a role in affecting the extreme rainfall in Shanghai through Rossby wave energy dispersion. This requires further observational and modeling studies.

The current observational analysis suggests that 2019 was an unique winter for being both extremely warm and wet. The circulation patterns in 2019 appeared different from those in other historical extreme warm or rainy winters during the past 30 years. The analysis results may be instructive for operational seasonal forecast in Shanghai. The tropical precipitation signals and associated SST anomaly patterns may be regarded as an important predictor for winter temperature and precipitation forecast in Shanghai, as such signals often persisted from the preceding season. In addtion to the precipitation anomalies in the tropics, heating signals from North Atlantic may also help enhance the seasonal predictability.

The time series of standardized tempearature shows a linear warming trend (Fig.

6a). To clarify the effect of global warming on anomalous temperature (~2.5) in 2019, the temperature with linear trend removed is also calculated (figure not shown) and 2019 winter is still the highest (~2.0) during the last 30 years. Therefore, the internal variability of temperature is more essential.

A recent study suggested the role of the Arctic sea ice in affecting the seasonal forecast of the EAWM (Zhang et al., 2020). Thus it is desirable to consider this effect in the future study. Another issue is whether there existed other forcing for the formation of the dipole circulation pattern during 3 extreme rainy winters. A further in-dpeth study is needed to understand these issues.

Acknowledgements: This study is jointly supported by NSFC grants 42088101 and 41875069, China Special Project for Forecasters CMAYBY2020-040, NSF grant AGS-20-06553, and NOAA grant NA18OAR4310298. This is SOEST contribution number 12345, IPRC contribution number 1234 and ESMC number 123.

Reference

Chen, W. and Zhou, Q. (2012) Modulation of the Arctic Oscillation and the East Asian winter climate relationships by the 11-yr solar cycle. *Adv. Atmos. Sci.* **29**: 217–226.

Gill, A.E. (1980) Some simple solutions for heat-induced tropical circulation. *Quart. J. Roy. Meteor. Soc*. **106**: 447-462.

He, S.P., Gao, Y.Q., Li, F., Wang, H.J. and He, Y.C. (2017) Impact of Arctic Oscillation on the East Asian climate: A review. *Earth Sci. Rev*. **164**: 48-62.

Huang, R.H., Cai, R.S., Chen, J.L. and Zhou, L.T. (2006) Interdecaldal variations of drought and flooding disasters in China and their association with the East Asian climate system. *Chin. J. Atmos. Sci.* **30**: 730–743. (in Chinese)

Jiang, L. and Li, T. (2019) Relative roles of El Niño-induced extratropical and tropical forcing in generating Tropical North Atlantic (TNA) SST anomaly. *Clim. Dyn.* **53**(7-8): 3791-3804.

Kanamitsu, M., Ebisuzaki, W., Woollen, J., Yang, S.K., Hnilo, J.J., Fiorino, M. and Potter, G.L. (2002) NCEP-DOE AMIP-II Reanalysis (R-2). *Bull. Am. Meteorol. Soc*. **83**(11): 1631-1643.

Kim, J.W., Yeh, S.W. and Chang, E.C. (2014) Combined effect of El Niño-Southern Oscillation and Pacific Decadal Oscillation on the East Asian winter monsoon. *Clim. Dyn*. **42**(3-4): 957-971.

Lee, S., Kim, S., Jhun, J., Ha, K. and Seo, Y. (2013) Robust warming over East Asia during the boreal winter monsoon and its possible causes. *Environ. Res. Lett*. **8**: 034001.

Li, T., Wang, B., Chang, C.P. and Zhang, Y. (2003) A theory for the Indian Ocean dipole-zonal mode. *J. Atmos. Sci.* **60**: 2119–2135.

Li, T., Wang, B., Wu, B., Zhou, T., Chang, C.P. and Zhang, R. (2017) Theories on Formation of an Anomalous Anticyclone in Western North Pacific during El Niño: A review. *J. Meteorol. Res.* **31**: 987-1006.

Liu, Y., Hu, Z.Z. and Wu, R. (2020) Was the Extremely Wet Winter of 2018/19 in the Lower Reach of the Yangtze River Driven by ENSO? *Int. J. Climatol.* 1-17. In

press.

Roeckner, E., Arpe, E., Bengtsson, L., Christoph, M., Claussen, M., Dümenil, L., Esch, M., Giorgetta, M., Schlese, U. and Schulzweida, U. (1996) The atmospheric general circulation model ECHAM4: Model description and simulation of present-day climate. *Max-Planck-Institut für Meteorologie Report Series 218. Technical Report, Max-Planck-Institut für Meteorologie*, 99pp.

Rogers, J.C. (1981) The North Pacific oscillation *J. Climatol*, **1**: 39–57.

Sha, Y., Shi, Z., Liu, X. and An, Z. (2015) Distinct impacts of the Mongolian and Tibetan Plateaus on the evolution of the East Asian monsoon. *J. Geophys. Res. Atmos.* **120**(10): 4764-4782.

Sun, Y.B., Clemens, S.C., Morrill, C., Lin, X., Wang, X. and An, Z. (2012) Influence of Atlantic meridional overturning circulation on the East Asian winter monsoon. *Nat. Geosci.*

Suo, L.L., Tan, B.K. and Huang, J.Y. (2009) Further exploration on causes of temperature anomalies associated with the abnormal northern annular mode. *Chin. Sci. Bull*. **54**: 2101–2106.

Takaya, K. adn Nakamura, H. (2001) A formulation of a phase-independent wave-activity flux for stationary and migratory quasi-geostrophic eddies on a zonally varying basic flow. *J. Atmos. Sci.* **58**: 608–627.

Tan, B.K. and Chen, W. (2014) Progress in the Study of the Dynamics of Extratropical Atmospheric Teleconnection Patterns and Their Impacts on East Asian Climate. *J. Meteoro. Res.* **028**(005): 780-802.

Ueda, H., Kamae, Y., Hayasaki, M., Kitoh, A., Watanabe, S., Miki, Y. and Kumai, A. (2015) Combined effects of recent Pacific cooling and Indian Ocean warming on the Asian monsoon. *Nat. Commun*. **6**: 8854.

Wallace, J.M. and Gutzler, D.S. (1981) Teleconnections in the geopotential height field during the Northern Hemisphere winter. *Mon. Wea. Rev*. **109**: 784–812.

Wang, B., Wu, R. and Fu, X. (2000) Pacific-East Asian teleconnection: how does ENSO affect East Asian climate? *J. Clim*. **13**: 1517–36.

Wang, L., Chen, W., Fong, S. and Leong, K. (2011) The seasonal march of the North Pacific Oscillation and its association with the interannual variations of China's climate in boreal winter and spring. *Chin. J. Atmos. Sci.* **35**: 393–402. (in Chinese)

Wang, L. and Feng, J. (2011) Two major modes of the wintertime precipitation over China. *Chin. J. Atmos. Sci.* **35**(6): 1105–1116.

Wang, L., Li, T., Maloney, E. and Wang, B. (2017) Fundamental causes of propagating and nonpropagating MJOs in MJOTF/GASS models. *J. Clim.* **30**(10): 3743-3769.

Wang, W., Xin, F., Pan, X., Zhang, Y. and Li, T. (2020) Seasonal and sub-seasonal circulation anomalies associated with persistent rainy days in 2018/2019 winter in Shanghai, *China. J. Meteor. Res.* **34**(2): 304–314.

Wen, M., Yang, S., Kumar, A. and Zhang, P.Q. (2009) An analysis of the large-scale climate anomalies associated with the snowstorms affecting China in January 2008. *Mon. Wea. Rev.* **137**: 1111–1131.

Wu, B., Zhou, T.J. and Li, T. (2017) Atmospheric dynamic and thermodynamic processes driving the western North Pacific anomalous anticyclone during El Niño. Part I: Maintenance mechanisms. *J. Clim*. **30**: 9621-9635.

Wu, B.Y. and Wang, J. (2002) Winter Arctic Oscillation, Siberian high and East Asian winter monsoon. *Geophys. Res. Lett.* **29**: 3-1-3-4.

Wu, Z.W., Wang, B., Li, J.P. and Jin, F.F. (2009) An empirical seasonal prediction model of the East Asian summer monsoon using ENSO and NAO. *J. Geophys. Res*. **114**: D18120.

Xie, P. and Arkin, P.A. (1997) Global precipitation: A 17-year monthly analysis based on gauge observations, satellite estimates, and numerical model outputs. *Bull. Amer. Meteor. Soc*. **78**: 2539-2558.

Zhang, P., Wu, Z., Li, J. and Xiao, Z. (2020) Seasonal prediction of the northern and southern temperature modes of the East Asian winter monsoon: the importance of the Arctic sea ice. *Clim. Dyn*. **D14**.

Zhang, R., Jiang, D., Zhang, Z. and Yu, E. (2015) The impact of regional uplift of the Tibetan Plateau on the Asian monsoon climate. *Palaeogeogr. Palaeoclimatol.*

Palaeoecol. **417**: 137-150.

Zhang, R., Sumi, A. and Kimoto, M. (1996) Impact of El Niño on the East Asian monsoon: A diagnostic study of the 86–87 and 91–92 events, *J. Meteorol. Soc. Jpn*. **74**: 49–62.

Zhou, Q., Chen, W. and Zhou, W. (2013) Solar cycle modulation of the ENSO impact on the winter climate of East Asia. *J. Geophys. Res. Atmos*. **118**(11): 5111-5119.

Zhou, Q. (2013) Impacts of 11-year solar cycle on East Asian climate and its mechanism. *Ph. D. issertation, Institute of Atmospheric Physics, Chinese Academy of Sciences*, 112 pp. (in Chinese)

Zhu, Z., Li, T. and He, J. (2014) Out-of-phase relationship between boreal spring and summer decadal rainfall changes in southern China. *J. Clim*. **27**(3): 1083-1099.

Zhu, Z. and Li, T. (2016) A new paradigm for continental U.S. summer rainfall variability: Asia–North America teleconnection. *J. Clim*. **29**(20): 7313-7327.

Figure Captions

Figure 1 Time series of winter (December, January, February) mean surface air temperature (red line; ℃) and precipitation (grey bar, mm·day^{-1}) averaged over 11 main stations in Shanghai during 1990-2019.

Figure 2 The horizontal patterns of (a) 1000hPa temperature (shading; ℃), 850hPa wind (vector; m·s^{-1}) and geopotential height (green contour; m) anomaly fields, (b) 1000hPa specific humidity (shading; g·kg^{-1}) and 500hPa vertical velocity (contour; Pa·s^{-1}) anomaly fields, and (c) 1000hPa-850hPa integrated MSE (shading; J·kg^{-1}) anomaly field averaged in 2019 winter. Letter "C" and "A" denote anomalous cyclonic and anticyclonic centers.

Figure 3 The horizontal patterns of (a) the mean temperature advection (shading; $\times10^{-5}$ ℃·s^{-1}) by anomalous wind (vector; m·s^{-1}) at 1000hPa and (b) the mean moisture advection (shading; $\times10^{-5}$ g·(kg·s)$^{-1}$) by anomalous wind (vector; m·s^{-1}) at 1000hPa.

Figure 4 (a) Rossby wave activity flux (purple vector; m^2·s^{-2}) and anomalous geopotential height (shading; m) and wind fields (black vector; m·s^{-1}) at 200hPa, (b) precipitation anomaly (shading; mm·day^{-1}) and (c) SSTA during 2019 winter.

Figure 5 Anomalous geopotential height (contour; m) and wind fields (vector; m·s^{-1}) at 200hPa in response to (a) the combined heating anomalies (shading; ℃·day^{-1}) in the Indian Ocean (10°S-20°N, 40°-80°E) and North Atlantic (50°-65°N, 10°W-10°E), (b) the heating anomaly (shading; ℃·day^{-1}) in the Indian Ocean, and (c) the heating anomaly (shading; ℃·day^{-1}) over North Atlantic. Red and blue contours denote positive and negative values. Letter "C" and "A" denote anomalous cyclonic and anticyclonic centers.

Figure 6 The time series of standardized (a) temperature and (b) precipitation during

1990-2019.

Figure 7 Composites of (a) anomalous 1000hPa temperature (shading; ℃) and 850hPa wind (vector; $m \cdot s^{-1}$) and geopotential height (blue contour; m) fields, (b) Rossby wave activity flux (purple vector; $m^2 \cdot s^{-2}$), geopotential height (shading; m) and wind anomaly fields (black vector; $m \cdot s^{-1}$) at 200hPa, and (c) precipitation anomaly (shading; $mm \cdot day^{-1}$) during 5 extreme warm years (1998, 2000, 2001, 2006 and 2016). Letter "C" and "A" denote anomalous cyclonic and anticyclonic centers. Dots denote the shading passing the significance of 95% using bootstrap test.

Figure 8 Simulated anomalous geopotential height (contour; m) and wind fields (vector; $m \cdot s^{-1}$) at 200hPa in response to (a) positive heating anomaly (shading; $℃ \cdot day^{-1}$) over the Maritime Continent (10°S-20°N, 90°-160°E) and North Atlantic (50°-65°N, 10°W-15°E), with negative heating in Indian Ocean (10°S-20°N, 50°-90°E); (b) only positive heating in Maritime Continent; (c) only negative heating in Indian Ocean; (d) only positive heating in North Atlantic. Red and blue contours denote positive and negative values. Letter "C" and "A" denote anomalous cyclonic and anticyclonic centers.

Figure 9 Composite patterns of (a) 1000hPa temperature (shading; ℃) and 850hPa wind (vector; $m \cdot s^{-1}$) and geopotential height (brown contour; m) fields, (b) 1000hPa specific humidity (shading; $g \cdot kg^{-1}$) and 500hPa vertical velocity (contour; $Pa \cdot s^{-1}$) and (c) 1000hPa-850hPa integrated MSE (shading; $J \cdot kg^{-1}$) anomaly fields for the three extreme rainy winters (1997, 2004 and 2018). Letter "C" and "A" denote anomalous cyclonic and anticyclonic centers. Dots denote shading passing the significance level of 95% using bootstrap test.

Figure 10 Composite patterns of (a) Rossby wave activity flux (purple vector; $m^2 \cdot s^{-2}$) and anomalous geopotential height (shading; m) and wind fields at 200hPa (black vector; m·s-1) and (b) precipitation anomaly (shading; mm·day-1) during the three

extreme rainy winters (1997, 2004 and 2018). Letter “C” and “A” denote anomalous cyclonic and anticyclonic centers. Dots denote the shading passing the significance of 95% using bootstrap test.

Figure 11 Anomalous geopotential height (contour; m) and wind fields (vector; $m \cdot s^{-1}$) at 200hPa response to (a) negative heating (shading; $℃ \cdot day^{-1}$) in Maritime Continent (10°S-20°N, 70°-160°E) and positive heating (shading; $℃ \cdot day^{-1}$) in western Indian Ocean (10°S-15°N, 30°-70°E); (b) only negative heating in Maritime Continent; (c) only positive heating in western Indian Ocean. Solid red lines and dashed blue lines denote positive and negative values. Letter “C” and “A” denote the anomalous cyclonic and anticyclone center.

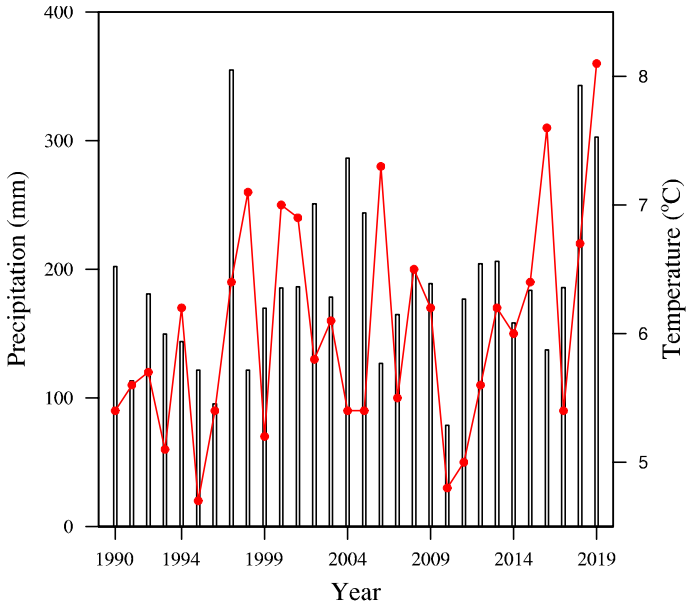

Figure 1 Time series of winter (December, January, February) mean surface air temperature (red line; ℃) and precipitation (grey bar, mm·day^{-1}) averaged over 11 main stations in Shanghai during 1990-2019.

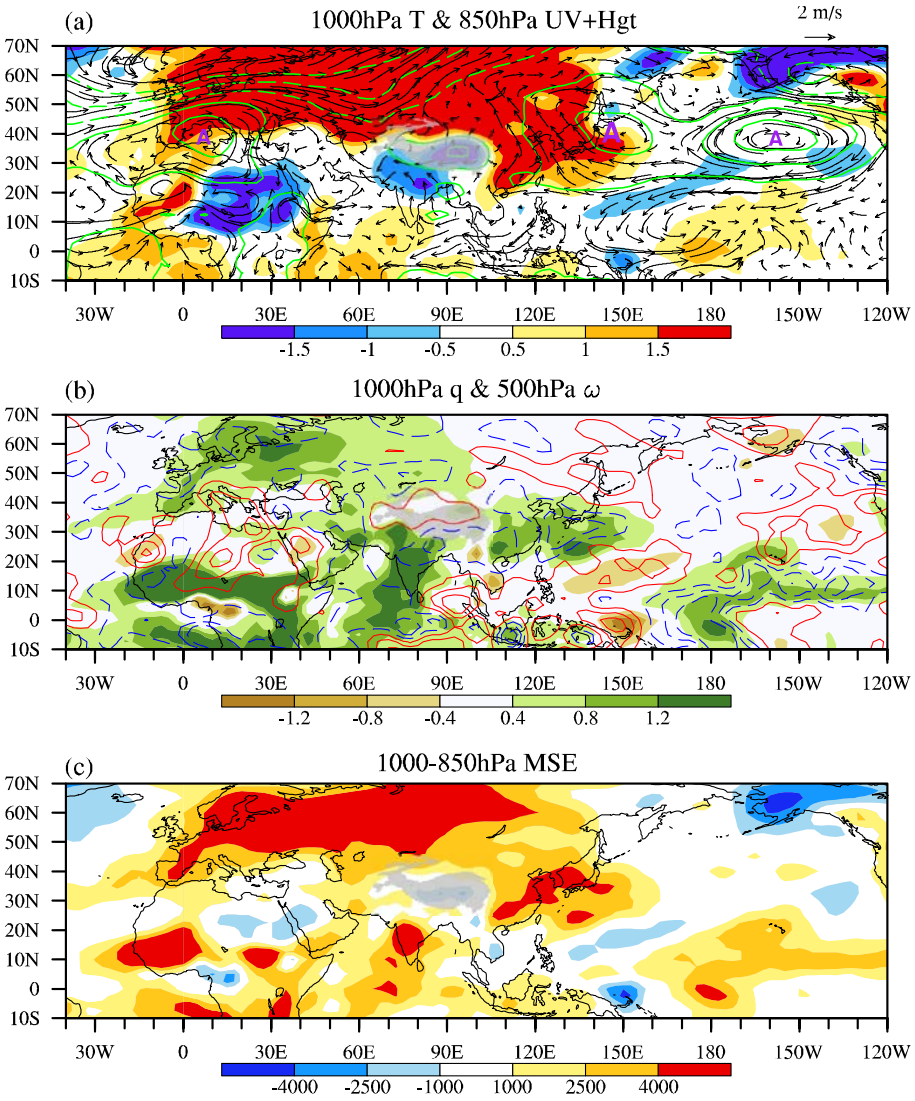

Figure 2 The horizontal patterns of (a) 1000hPa temperature (shading; ℃), 850hPa wind (vector; $m \cdot s^{-1}$) and geopotential height (green contour; m) anomaly fields, (b) 1000hPa specific humidity (shading; $g \cdot kg^{-1}$) and 500hPa vertical velocity (contour; $Pa \cdot s^{-1}$) anomaly fields, and (c) 1000hPa-850hPa integrated MSE (shading; $J \cdot kg^{-1}$) anomaly field averaged in 2019 winter. Letter "C" and "A" denote anomalous cyclonic and anticyclonic centers.

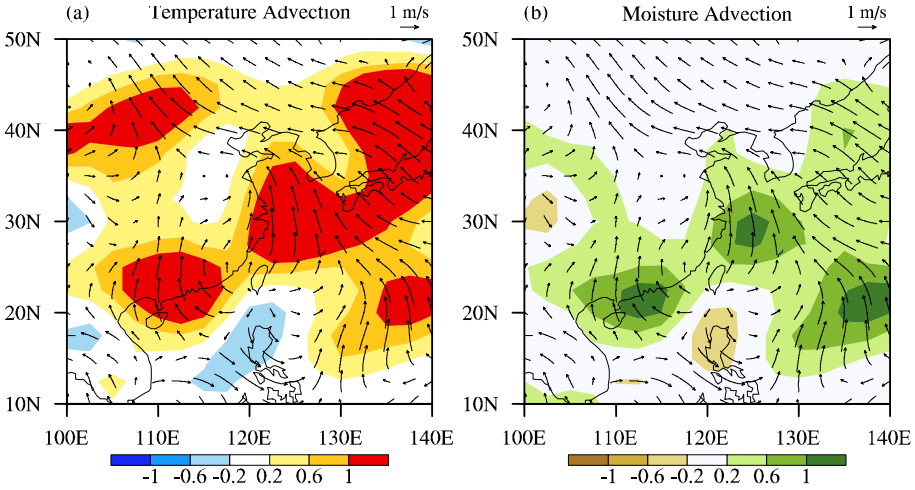

Figure 3 The horizontal patterns of (a) the mean temperature advection (shading; $\times 10^{-5}$ ℃·s^{-1}) by anomalous wind (vector; m·s^{-1}) at 1000hPa and (b) the mean moisture advection (shading; $\times 10^{-5}$ g·(kg·s)$^{-1}$) by anomalous wind (vector; m·s^{-1}) at 1000hPa.

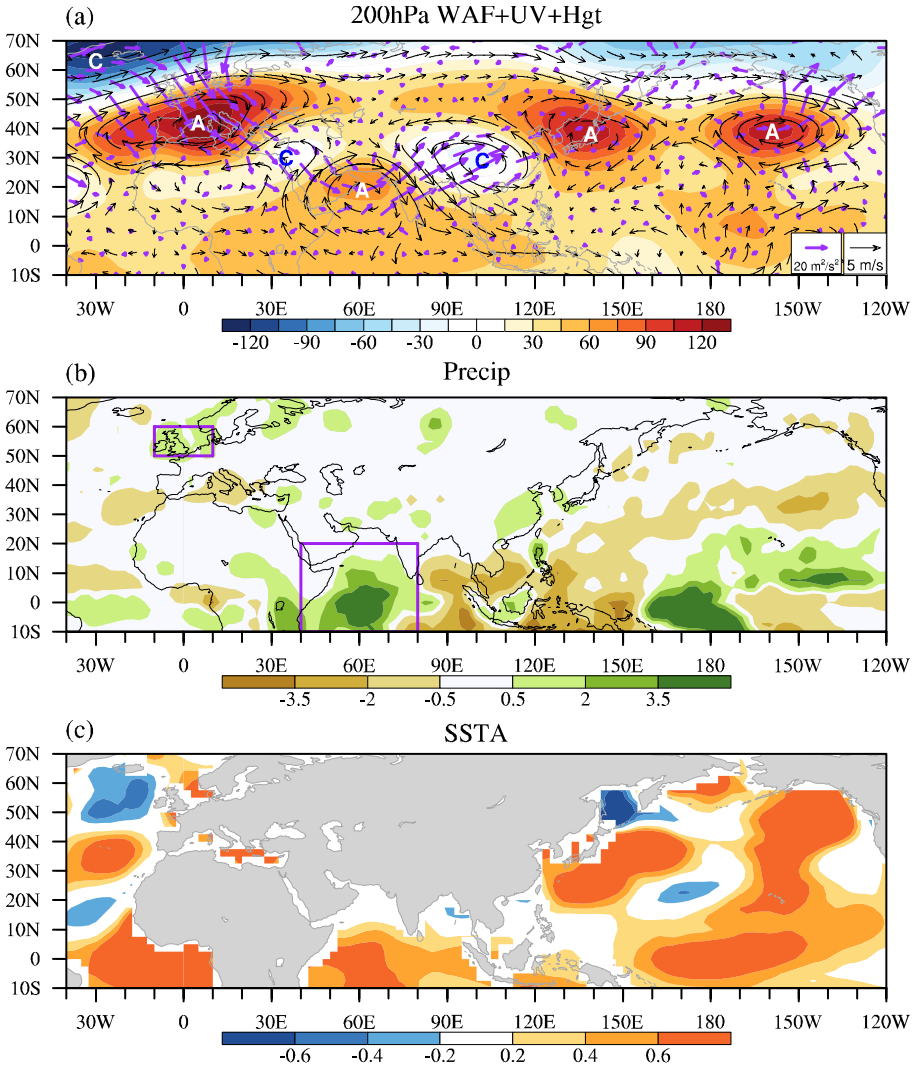

Figure 4 (a) Rossby wave activity flux (purple vector; $m^2 \cdot s^{-2}$) and anomalous geopotential height (shading; m) and wind fields (black vector; $m \cdot s^{-1}$) at 200hPa, (b) precipitation anomaly (shading; $mm \cdot day^{-1}$) and (c) SSTA during 2019 winter.

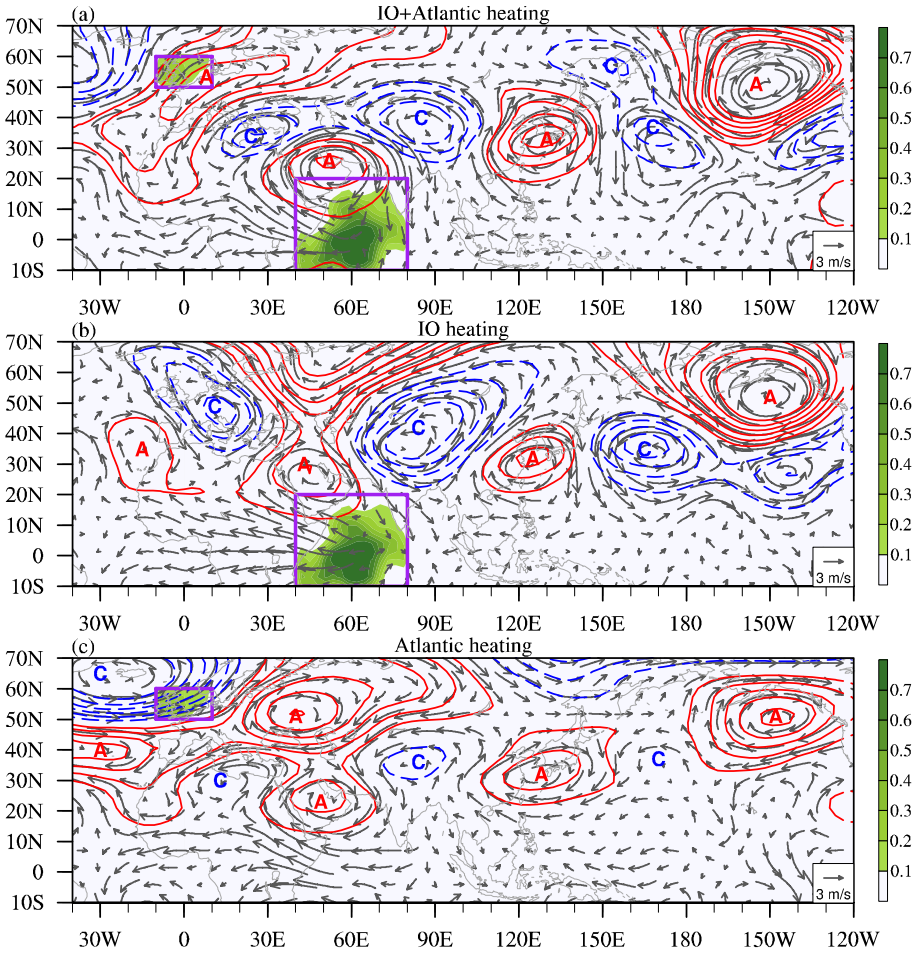

Figure 5 Anomalous geopotential height (contour; m) and wind fields (vector; m·s^{-1}) at 200hPa in response to (a) the combined heating anomalies (shading; ℃·day^{-1}) in the Indian Ocean (10°S-20°N, 40°-80°E) and North Atlantic (50°-65°N, 10°W-10°E), (b) the heating anomaly (shading; ℃·day^{-1}) in the Indian Ocean, and (c) the heating anomaly (shading; ℃·day^{-1}) over North Atlantic. Red and blue contours denote positive and negative values. Letter "C" and "A" denote anomalous cyclonic and anticyclonic centers.

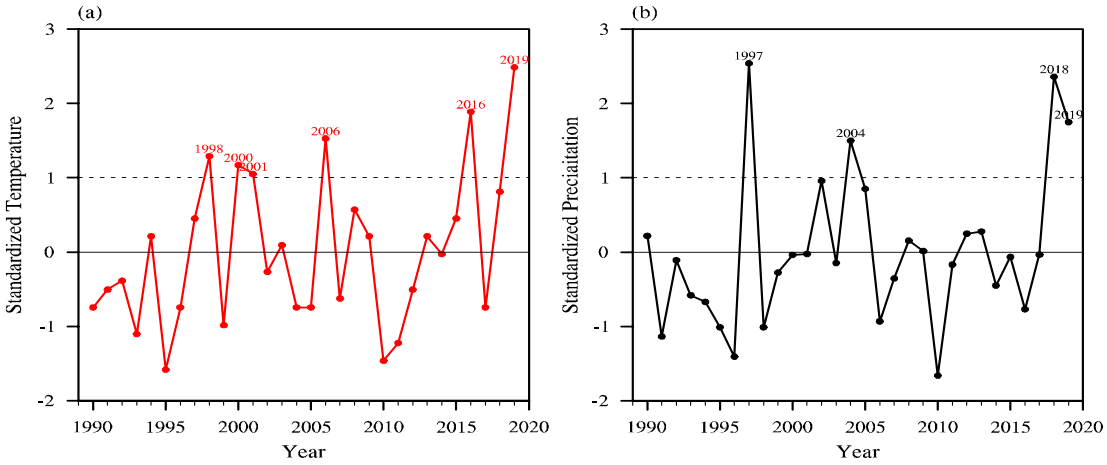

Figure 6 The time series of standardized (a) temperature and (b) precipitation during 1990-2019.

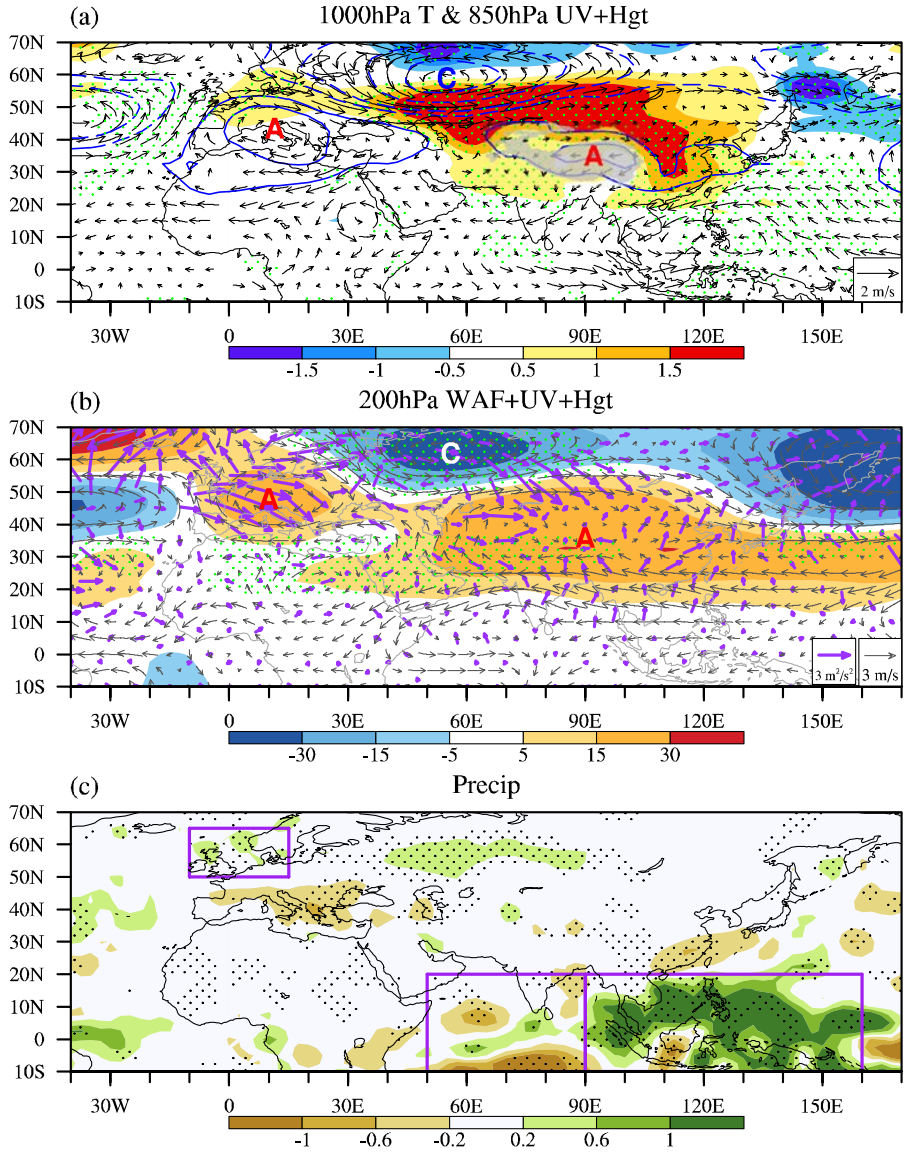

Figure 7 Composites of (a) anomalous 1000hPa temperature (shading; ℃) and 850hPa wind (vector; $m \cdot s^{-1}$) and geopotential height (blue contour; m) fields, (b) Rossby wave activity flux (purple vector; $m^2 \cdot s^{-2}$), geopotential height (shading; m) and wind anomaly fields (black vector; $m \cdot s^{-1}$) at 200hPa, and (c) precipitation anomaly (shading; $mm \cdot day^{-1}$) during 5 extreme warm years (1998, 2000, 2001, 2006 and 2016). Letter "C" and "A" denote anomalous cyclonic and anticyclonic centers. Dots denote the shading passing the significance of 95% using bootstrap test.

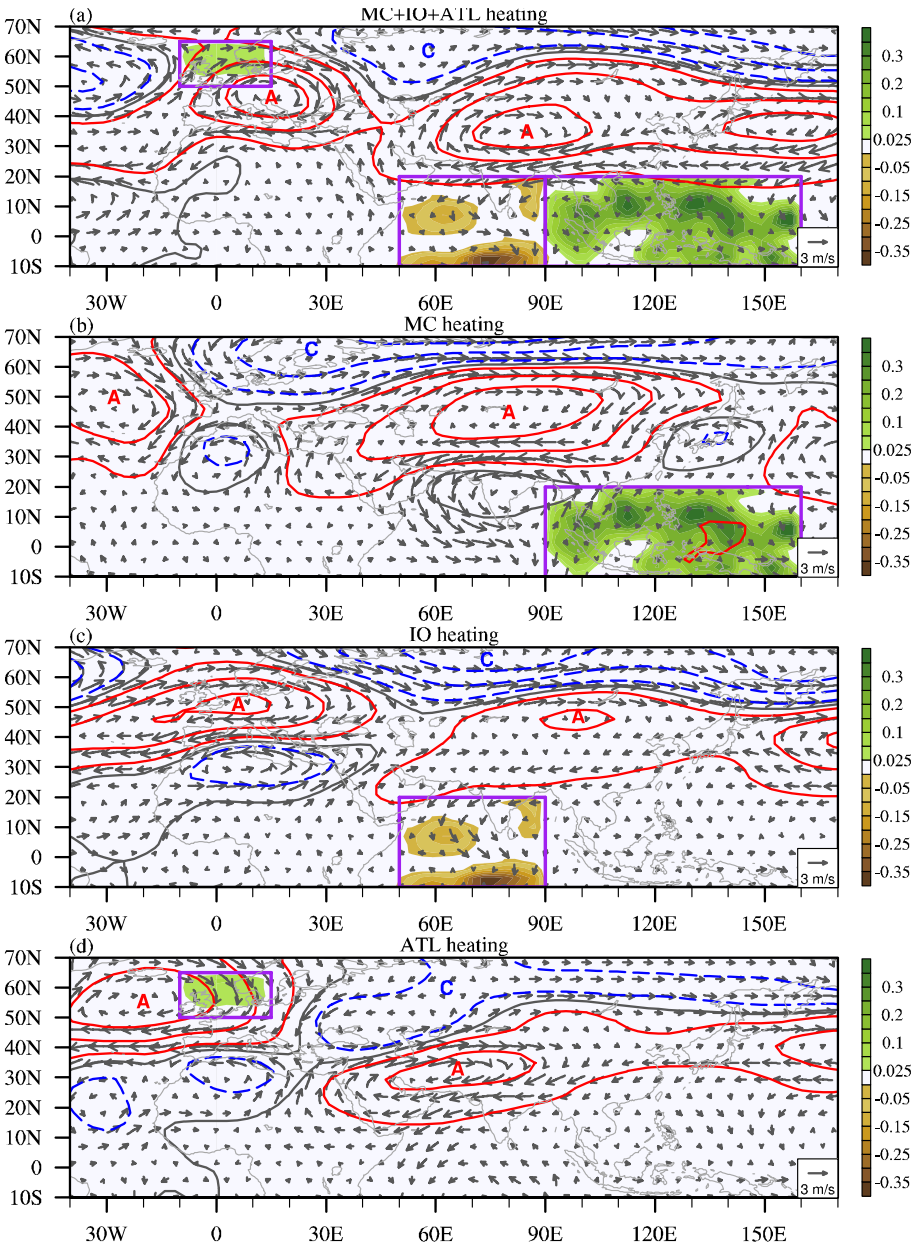

Figure 8 Simulated anomalous geopotential height (contour; m) and wind fields (vector; $m \cdot s^{-1}$) at 200hPa in response to (a) positive heating anomaly (shading; $℃ \cdot day^{-1}$) over the Maritime Continent (10°S-20°N, 90°-160°E) and North Atlantic (50°-65°N, 10°W-15°E), with negative heating in Indian Ocean (10°S-20°N, 50°-90°E); (b) only positive heating in Maritime Continent; (c) only negative heating in Indian Ocean; (d) only positive heating in North Atlantic. Red and blue contours denote positive and negative values. Letter "C" and "A" denote anomalous cyclonic and anticyclonic centers.

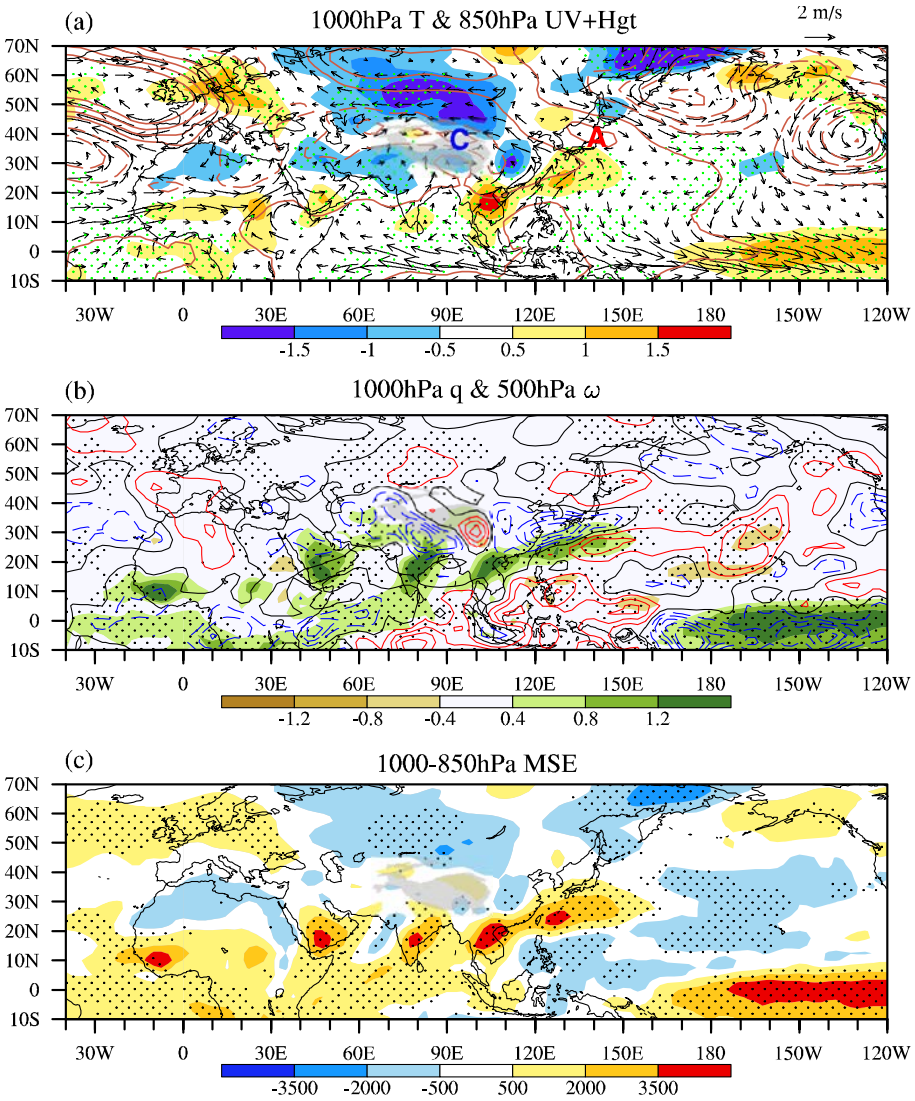

Figure 9 Composite patterns of (a) 1000hPa temperature (shading; ℃) and 850hPa wind (vector; $m \cdot s^{-1}$) and geopotential height (brown contour; m) fields, (b) 1000hPa specific humidity (shading; $g \cdot kg^{-1}$) and 500hPa vertical velocity (contour; $Pa \cdot s^{-1}$) and (c) 1000hPa-850hPa integrated MSE (shading; $J \cdot kg^{-1}$) anomaly fields for the three extreme rainy winters (1997, 2004 and 2018). Letter "C" and "A" denote anomalous cyclonic and anticyclonic centers. Dots denote shading passing the significance level of 95% using bootstrap test.

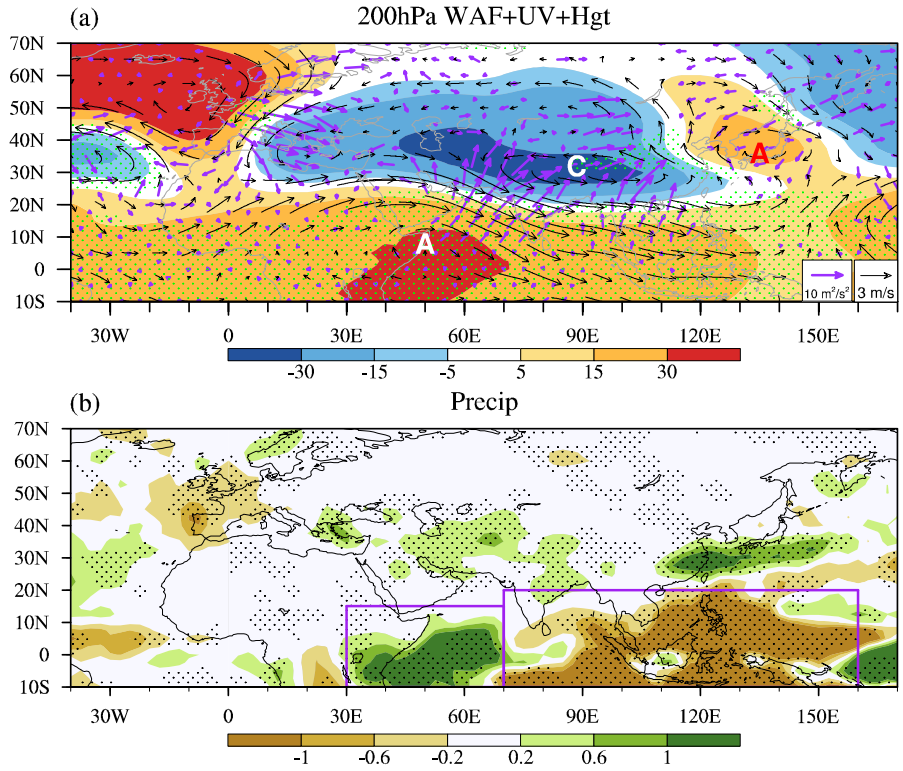

Figure 10 Composite patterns of (a) Rossby wave activity flux (purple vector; $m^2 \cdot s^{-2}$) and anomalous geopotential height (shading; m) and wind fields at 200hPa (black vector; $m \cdot s^{-1}$) and (b) precipitation anomaly (shading; $mm \cdot day^{-1}$) during the three extreme rainy winters (1997, 2004 and 2018). Letter "C" and "A" denote anomalous cyclonic and anticyclonic centers. Dots denote the shading passing the significance of 95% using bootstrap test.

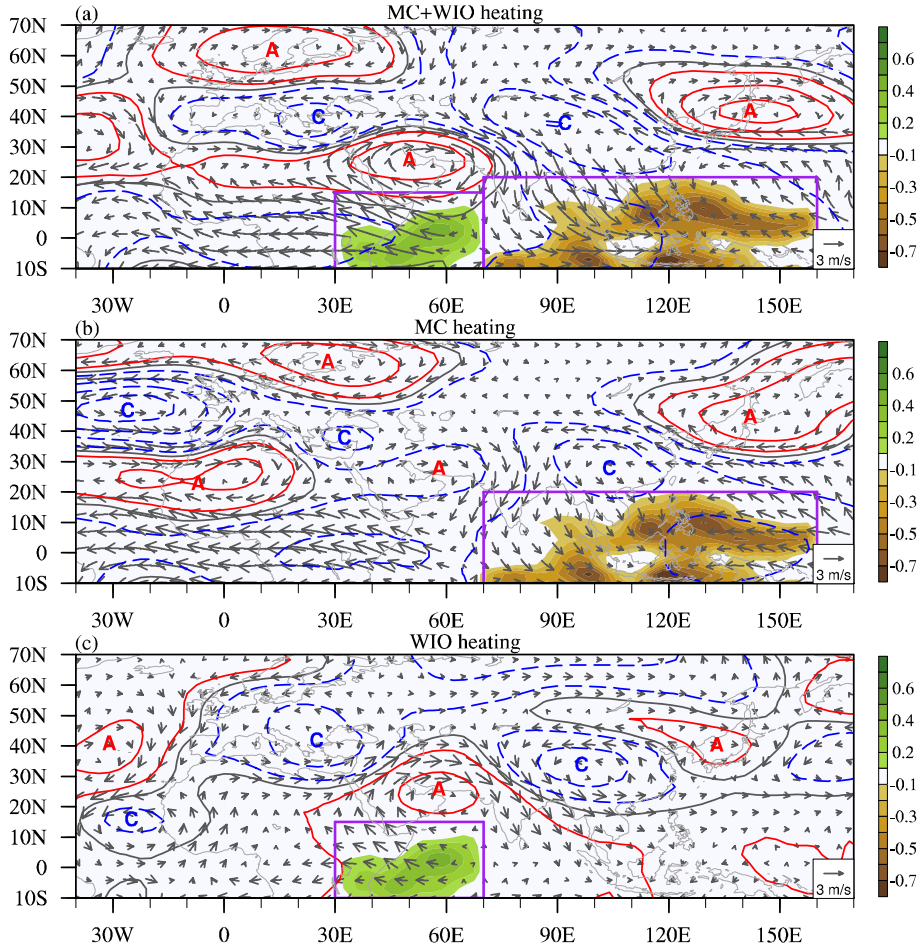

Figure 11 Anomalous geopotential height (contour; m) and wind fields (vector; m·s^{-1}) at 200hPa response to (a) negative heating (shading; ℃·day^{-1}) in Maritime Continent (10°S-20°N, 70°-160°E) and positive heating (shading; ℃·day^{-1}) in western Indian Ocean (10°S-15°N, 30°-70°E); (b) only negative heating in Maritime Continent; (c) only positive heating in western Indian Ocean. Solid red lines and dashed blue lines denote positive and negative values. Letter "C" and "A" denote the anomalous cyclonic and anticyclone center.

Cause of an extreme warm and rainy winter in Shanghai in 2019

Xiao Pan, Wei Wang, Tim Li*, Fei Xin and Jinhua Yu*

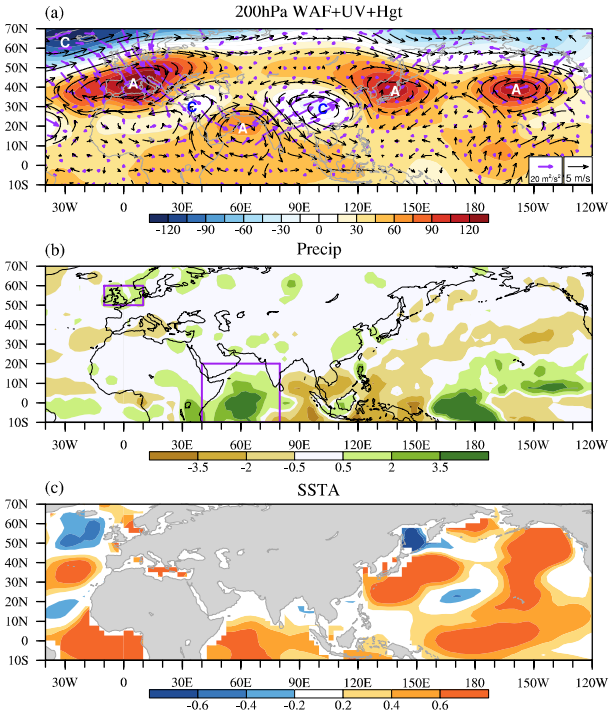

Observational diagnosis shows that the extreme warm and rainy winter in Shanghai in 2019 arose from southerly anomalies associated with an anticyclone, which was attributed to V-shaped upper-tropospheric Rossby wave activity fluxes, originated from the North Atlantic and tropical Indian Ocean. Numerical model experiments indicate that the anomalous heat source in the tropical Indian Ocean played a dominant role (~65%) in causing the local anomalous circulation, while the heating in North Atlantic also played a role (~35%). Further analysis revealed that an extreme warm winter in the past did not coincide with an extreme wet winter.